Analysis of Aluminum Resistance Spot Welding Processes Using Coupled Finite Element Procedures

Incrementally coupled finite element procedures that simulate the resistance spot welding process are suitable for analyzing a variety of important weld parameters

BY X. SUN AND P. DONG

ABSTRACT. A comprehensive analysis procedure has been developed to perform the incrementally coupled thermal-electrical-mechanical analysis to simulate the resistance spot welding process of aluminum alloys. Because aluminum has high thermal conductivity, low melting temperature and low yield strength, deformation resulting from resistance spot welding is expected to be more severe than for steel. Compared with most of the published work in this area, this paper takes into account the incremental changes in sheet-deformed shape, contact area and current density profile as well as large deformation effects. The present analysis procedures consider electrical contact resistivities to be not only functions of contact temperature but also functions of pressure. Joule heating at the contact surfaces is computed using an equivalent surface heat generation concept.

This new procedure is suitable for analyzing many important parameters such as contact area changes, electrode movement and dynamic resistance, as well as other factors that contribute to weld quality such as weld size, weld indentation, sheet separation and weld residual stresses. It can also be used to study nugget development and analyze the mechanisms of electrode wear and weld cracking.

Introduction

Resistance spot welding (RSW) is commonly used in the automotive industry for joining thin sheet metals. With the rapid increase in the use of aluminum alloys for automotive body and structural components, a better understanding of aluminum spot welding processes has become necessary. Steel and aluminum alloys share many of the same process attributes for spot welding. However, the productivity of aluminum spot welding is lower than that of steel, and the control of weld quality is much more difficult. This is because aluminum alloys have higher thermal and electrical conductivity, and a higher welding current and electrode force are required to generate a desired weld nugget. The resulting thermo-mechanical conditions would, in turn, lead to faster electrode wear. Moreover, because of the very high energy input rate in welding aluminum and the approximately 7% volume increase of aluminum at its melting point, expulsion is frequently observed and undesirable nugget defects often result as a consequence of the loss of liquid metal.

Numerical modeling has proven to be an effective tool in understanding the RSW process in quantitative details. Greenwood (Ref. 1) investigated the temperature distributions in spot welding by solving a two-dimensional boundary value problem using the finite difference method. Han, *et al.* (Ref. 2), conducted a similar study but allowed for variations in the physical properties of the workpiece. Cho and Cho (Ref. 3) developed a finite difference scheme to predict the temperature and voltage distribution incorporating the thermoelectric interaction at the interface in the weldment. Several authors have approached a similar problem by using sequentially coupled finite element models, which simulate squeezing cycle and welding cycle in sequential order, to address different aspects of the RSW process such as nugget growth, electrode design and electrode wear. Among them are Nied (Ref. 4); Tsai, *et al.* (Ref. 7); Sheppard (Ref. 8); Murakawa (Ref. 9); and Dong, *et al.* (Ref. 10). Most of these models were used to simulate spot welding with flat-tipped electrodes, and assume the contact radii between the electrode-sheet interface and faying interface remain constant throughout the entire welding process. However, since the contact radii are the manifestations of the process dynamics and the results of the competition between thermal expansion and electrode squeezing force, they vary during the entire welding process. This is particularly true for domed electrodes, which are used most often in RSW of aluminum alloys. To incorporate the contact area changes for domed electrodes, Browne, *et al.* (Refs. 5, 6), developed an analysis procedure in which both finite element and finite difference methods were used. In their analyses, dome-shaped electrode tips were only used in mechanical analysis. Electro-thermal analysis still used a flat electrode tip and only contact radii of the interfaces were passed from mechanical analysis to the electro-thermal analysis.

Spot welding is a strongly coupled electrical, thermal and mechanical process. Since aluminum has high thermal conductivity, low melting temperature and low yield strength, the associated deformation during welding, final distortion (indentation) and sheet separation are expected to be more severe

KEY WORDS

Resistance Spot Welding
Thermal-Electrical-Mechanical Analysis
Electrode Movement
Dynamic Resistance
Nugget Formation
Weld Cracking

X. SUN and P. DONG are with the Battelle Memorial Institute, Columbus, Ohio.

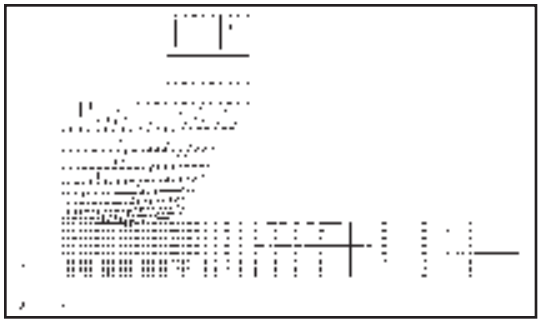

Fig. 1 — Typical finite element model.

than for steel. Therefore, the above-mentioned approaches used in the open literature are no longer sufficient for obtaining the complicated process details associated with aluminum RSW with a domed electrode.

In this paper, the mathematical formulation with respect to the coupled effects of electrical-thermal-mechanical phenomena associated with the resistance spot welding process is briefly presented. Its finite element implementation, which takes advantage of commercial codes, *e.g.*, ABAQUS, is then discussed within the context of incrementally coupled electrical-thermal-mechanical procedures. Finally, a case study on welding of 5xxx series aluminum alloy sheets is presented in detail. Nugget formation and the associated dynamic interactions between different interfaces, as well as residual stress states, are discussed in light of the present results.

Theoretical Framework

Assuming no internal current source, the following is the governing differential equation for the electrical potential field:

$$\frac{\partial^2\varphi}{\partial x^2}+\frac{\partial^2\varphi}{\partial y^2}+\frac{\partial^2\varphi}{\partial z^2}=0 \qquad (1)$$

where $\varphi(x,y,z,t)$ is the electrical potential and x, y, z are the coordinates in the Cartesian coordinate system. Introducing Ohm's law, the variational form of Equation 1 reads as follows (Ref. 13):

$$\int_V \frac{\partial\delta\varphi}{\partial x}\cdot\sigma^E\cdot\frac{\partial\varphi}{\partial x}dV=\int_S \delta\varphi J dS \qquad (2)$$

where $\sigma^E(\theta,f^\alpha)$ is the electrical conductivity matrix, $\theta=\theta(x,y,z,t)$ represents temperature, which is a function of both time and coordinates, f^α are any predefined field variables and $J=-\mathbf{J}\cdot\mathbf{n}$ is the current density entering the control volume across S.

The general three-dimensional differential equation governing heat conduction with internal heat source follows:

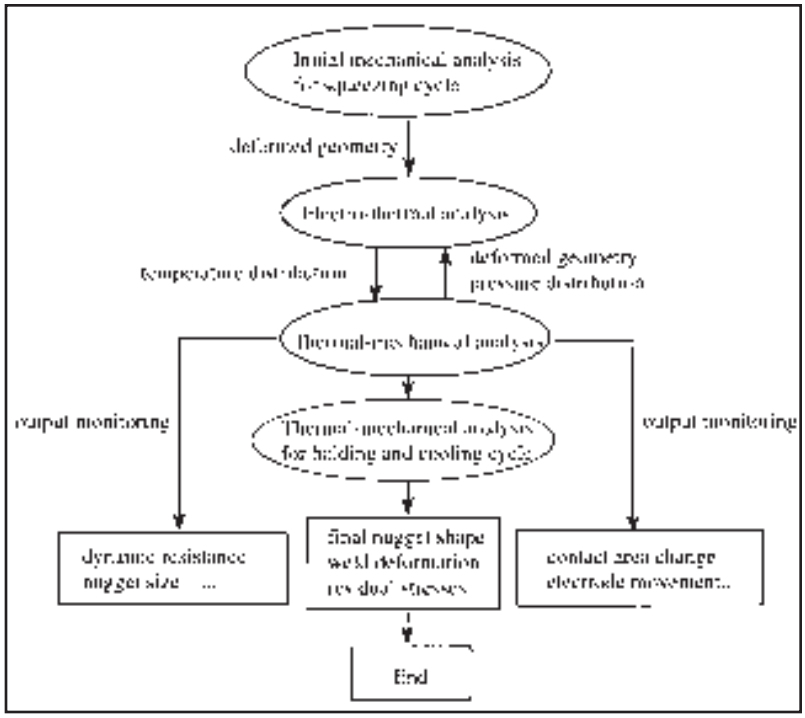

Fig. 2 — Analysis flow chart of the coupled electrical-thermal-mechanical analysis.

$$\frac{\partial}{\partial x}\left(k\frac{\partial\theta}{\partial x}\right)+\frac{\partial}{\partial y}\left(k\frac{\partial\theta}{\partial y}\right)+\frac{\partial}{\partial z}\left(k\frac{\partial\theta}{\partial z}\right)+\dot{Q}=\rho\frac{\partial U}{\partial t} \qquad (3)$$

where k and ρ are the material's thermal conductivity and density, respectively; Q is the internal heat generation rate per unit volume; and U is the internal energy. The variational form of Equation 3 using the standard Galerkin's approach is the following:

$$\int_V \rho\dot{U}\delta\theta dV+\int_V \frac{\partial\delta\theta}{\partial\mathbf{x}}\cdot\mathbf{k}\cdot\frac{\partial\theta}{\partial\mathbf{x}}dV=\int_V \partial\theta r dV+\int_S \delta\theta q dS \qquad (4)$$

where k is the thermal conductivity matrix, q is the heat flux per unit area of the body flowing into the body and r is the heat generated within the body due to Joule heating.

Dividing the total surface area S into S_p *and* S_i, which represent the surface on which the boundary conditions can be prescribed and the surface that interacts with nearby surfaces of other bodies, respectively, and denoting the rate of electrical energy dissipated by current flowing through a conductor as P_{ec}, Equations 2 and 4 become the following:

$$\int_V \frac{\partial\delta\varphi}{\partial x}\cdot\sigma^E\cdot\frac{\partial\varphi}{\partial x}dV=\int_{S_P}\delta\varphi J dS+\int_{S_i}\delta\varphi J dS \qquad (5)$$

and

$$\int_V \rho\dot{U}\delta\theta dV+\int_V \frac{\partial\delta\theta}{\partial x}\cdot k\cdot\frac{\partial\theta}{\partial x}dV=\int_V \delta\theta\eta_v P_{ec}dV+\int_{S_P}\delta\theta q dS+\int_{S_i}\delta\theta(q_c+q_r+q_{ec})dS \qquad (6)$$

In Equation 6, η_v is the energy conversion factor for the amount of electrical energy released as internal heat; q_c, q_r and q_{ec} represent heat conduction, radiation and heat generated on the interfaces (Ref. 13). The detailed discussions regarding J, q_c, q_r and q_{ec} will be presented in the next section.

In addition, localized temperature gradients due to heat generation and dissipation (see Equations 5 and 6) induce a thermo-mechanical response. The equilibrium conditions can be established using the theorem of virtual work, which states that a virtual change of the internal strain energy must be offset by an identical change in external virtual work due to the applied loads:

$$\delta U = {}_V\tau\delta\varepsilon dV = {}_S T\delta u dS = \delta V \qquad (7)$$

where δU is the virtual change of internal strain energy through the virtual strain $\delta\varepsilon$ and δV is the virtual change in external work done by traction **T** through virtual displacement δ**u**. In Equation 7, the stress components τ can be related to the strain components ε through the constitutive equation $\tau = \mathbf{D}(\varepsilon - \varepsilon^{th})$ (ε^{th} is the thermal strain component), and the strain components ε can be related to the displacement components **u** through the strain-displacement matrix.

Equations 5–7 are now ready for finite element discretization, and potential field φ, temperature field θ and displacement vector **u** should be simultaneously solved as nodal variables in a coupled manner.

Finite Element Implementation

Although various numerical analysis procedures can be adopted in solving the aforementioned coupled problem, the finite element (FE) method is highly desirable due to its flexibility in dealing with complex applications. Because there are no commercial FE codes capable of solving Equations 5–7 in a fully coupled manner, an incrementally coupled finite element analysis procedure has been implemented in this study. By taking advantage of some of the existing electrical-thermal and thermal-mechanical analysis modules in commercial codes, Equations 5 and 6 can be readily solved at a given moment in time, and the resulting temperature history can be used as thermal load to establish the corresponding thermal-mechanical solution at that time.

The analysis procedures can be demonstrated by using the commercial finite element code ABAQUS. Without losing generality, a typical finite element mesh is shown in Fig. 1 where a quarter symmetry condition is assumed. First, the squeeze cycle is modeled by a mechanical analysis. Contact surface interactions between the electrode-sheet interfaces and faying interface are modeled by the concept of contact pairs. Results from the squeezing-cycle mechanical analysis, including deformed shape, contact pressure, contact radius, root opening, etc., are then passed onto the next step, the electrical-thermal analysis in which the welding current is applied. The electrical-thermal analysis module shares the same mesh and the element definition with the thermal-mechanical module, and the nodal coordinates and contact information are updated each increment. Unlike other approaches in which a layer of fictitious solid contact elements has to be introduced with a physical thickness (Refs. 4, 7) to represent the contact areas of electrode/sheet interface and faying interface, the surface interactions in this study are modeled using the concept of surface contact pairs (Refs. 13, 17, 18, 20). The detailed theoretical formulation for these surface contact pairs will be discussed in subsequent sections. The temperature distribution resulting from the previously mentioned electrical-thermal analysis is used next as the thermal loading conditions for the subsequent thermal-mechanical analysis. The deformed shape of the electrode and sheet assembly and the change in contact status at the end of the incremental thermal-mechanical analysis are then passed into the next increment of electrical-thermal analysis as input, where the heat generated from the applied current is again computed. This updating procedure repeats itself for a specific time increment until the entire welding cycle is totally completed. Temperature-dependent material properties and melting/solidification response during the holding and subsequent cooling stages are also considered, so the final weld residual stresses and distortions are also predicted.

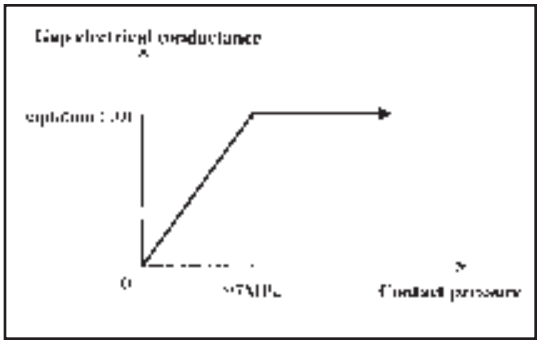

Fig. 3 — Illustration of gap electrical conductance calculation.

The flow chart of the analysis procedure is illustrated in Fig. 2. In Fig. 2, the analyses shown in the ovals are performed using different analysis modules in ABAQUS. The operations illustrated by arrows are performed by a series of Fortran user-interface subroutines. The entire analysis procedures were fully automated with the development of a Unix shell script.

Thermal-Mechanical Analysis

Uniformly distributed pressure for the given electrode force is applied to the top of the upper electrode. Contact pairs are set up between the electrode-to-sheet interface and the sheet-to-sheet faying interface, respectively. This ensures the surfaces in contact will not penetrate each other. The temperature history obtained from the electrical-thermal analysis is imposed as thermal loading. To improve convergence, softened surface properties

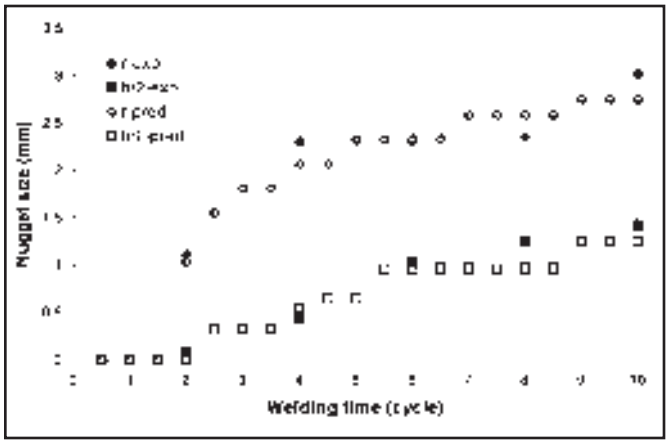

Fig. 4 — Nugget growth comparison between analysis results and experimental measurements.

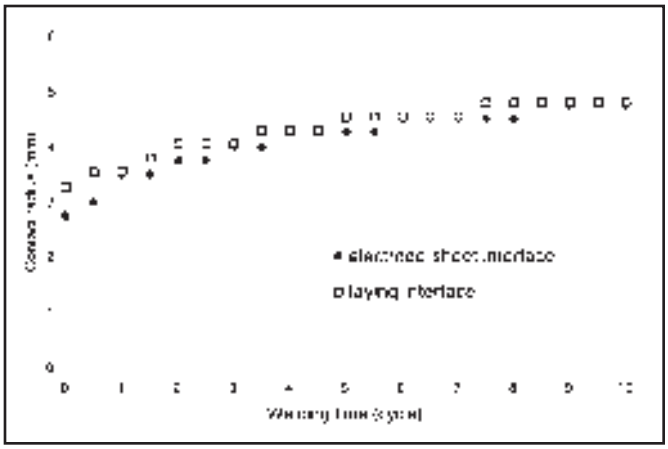

Fig. 5 — Predicted contact radius changes during welding.

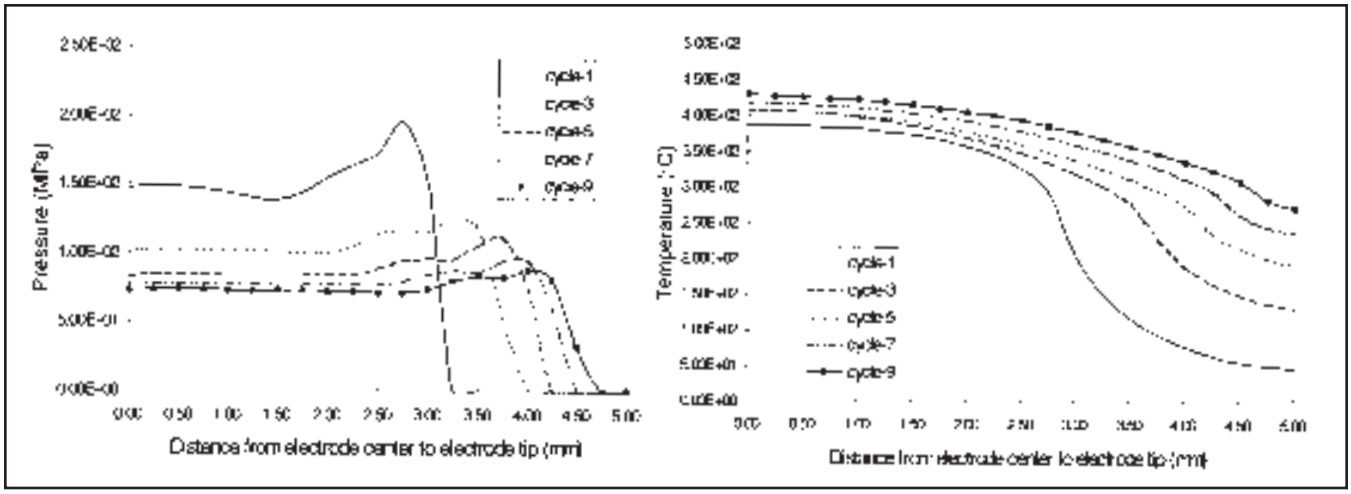

Fig. 6 — Pressure and temperature history on electrode-sheet interface.

are used and a small sliding effect is also included to simulate the relative slip between the electrode and workpiece due to the difference in their thermal expansion properties.

To simulate nugget formation effects at the faying surface, temperature history-dependent user subroutines are written to join the interface nodes as the nodal temperature reaches melting temperature. As a result, the corresponding residual stress state can also be predicted upon the completion of the cooling cycle.

Electrical-Thermal Analysis

The deformed configuration of the electrode and sheet assembly obtained from the previous thermal-mechanical analysis step is used as the input for electrical-thermal analysis. Contact radius and contact pressure obtained in the thermal-mechanical analysis are used to determine the width of the current passage and the electrical conductivity of the interfaces (Ref. 16). Once intimate contact is established, the electrical and thermal conductivity of the electrode-to-sheet interface is set to be the same as the bulk properties of aluminum (Refs. 5, 6). Properties of the faying interface are functions of both temperature and pressure (Refs. 12, 19). The surface interaction model includes heat conduction and radiation effects between the interface surfaces, and these interactions are handled using the concept of contact pairs. Heat conduction and radiation terms in Equation 6 are modeled by the following:

$$q_c = k_g(\theta_B - \theta), \qquad (7)$$

and

$$q_r = F_B(\theta_B - \theta^z)^4 - F(\theta - \theta^z)^4 \qquad (8)$$

where k_g is gap thermal conductance; F_B and F are constants; θ, θ_B and θ^z are temperature of the surface under consideration, temperature of the other surface and absolute-zero temperature, respectively. The electrical current flowing between the contact surface S_i in Equation 5 is modeled by (Ref. 13) the following:

$$J = \sigma_g(\varphi_A - \varphi_B) \qquad (9)$$

where σ_g is the gap electrical conductance and φ_A and φ_B are the electrical potentials at the two points on the contact surfaces.

Contact Electrical Conductance of the Faying Interface

As discussed by Browne, *et al.* (Refs. 5, 6), contact resistance plays an important role in the RSW process for aluminum. In this study, once contact was established

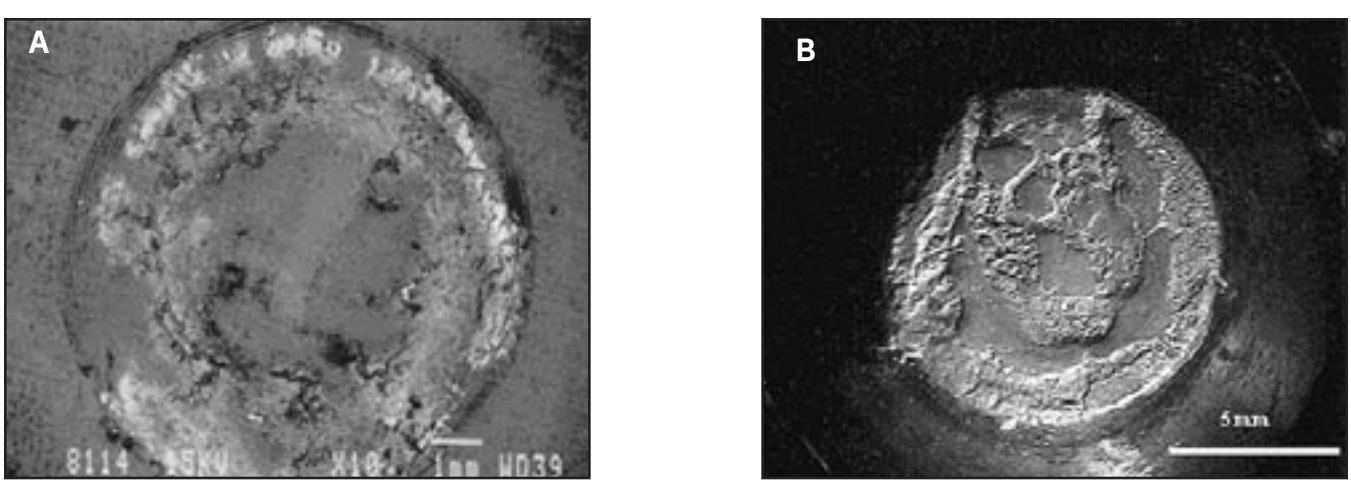

Fig. 7 — A — Backscatter electron image of the weld surface; B — photograph of a worn electrode face.

on the interface by the indication of contact pressure, the gap thermal conductance, k_g, is set to be equal to the thermal conductance of the aluminum workpiece with a characteristic length of the contact gap. The characteristic length of 0.1 mm is used in this work.

The contact electrical conductance σ_g is derived using the formulation provided by Li, *et al.* (Refs. 13, 16):

$$\sigma_g = \frac{1}{\rho h} = \frac{1}{R_c A_c} = \frac{I}{2\sqrt{L\left(T_s^2 - T_0^2\right)\pi r_c^2}} \qquad (10)$$

in which L is the Lorentz constant and T_s and T_0 are the maximum interface temperature and the bulk temperature in Kelvin. For most metals, L is found to be around 2.4 x 10^{-8}(V/K)^2. Note the assumption for the above resistivity formulation is that the entire interface area r^2_c is under intimate metallic contact. This assumption prompts the formulation of pressure dependency of the contact gap conductance since researchers have shown earlier the number of contact asperities increases almost proportionally with the increase of contact pressure before the entire interface is in metallic contact (Ref. 21). As a matter of fact, it is stated in the *Welding Handbook* (Ref. 12), that "resistance is roughly inversely proportional to the contact pressure." Vogler and Sheppard (Ref. 19) verified this statement by their experimental observations on steel. Their results revealed the contact resistance for bare mild steel follows the inversely proportional relation with respect to pressure before reaching a plateau value beyond a threshold pressure. This indicates the gap conductance should be roughly proportional to the contact pressure before reaching the value indicated by Equation 10. In this work, the threshold pressure value of the faying interface is set to the room temperature yield strength of the aluminum workpiece. If the gap interface pressure is greater than the threshold, the conductance is calculated by Equation 10. If the gap interface pressure is lower than the threshold, the gap conductance is obtained through linear interpolation as shown in Fig. 3.

To implement this formulation in the finite element simulation, the solidus temperature T_s of the interface is set to be 590°C. The contact radius r_c and contact gap pressure obtained from the previous thermal-mechanical analysis are extracted and used as input to the electrical-thermal analysis module through the option of "field variables." A user interface subroutine is then coded to calculate gap conductance based on nodal temperature, nodal pressure and total contact area according to Equation 10 and Fig. 3.

Table 1 — Welding Schedule

Current (kA)	Electrode Force	Squeeze Time	Weld Time	Hold Time
	(lb)	(cycle)	(cycle)	(cycle)
26.0	1100	60	10	30

A case study follows in which the modeling procedure described above is used to simulate the spot welding process of 5xxx series aluminum alloy. Excellent predictions are obtained compared with the experimentally observed nugget size and dynamic resistance, and this serves as a validation of the model. Final weld indentation and weld residual stresses are also obtained using this analysis procedure. The simulation not only provides useful insight on nugget growth history but it also provides valu-

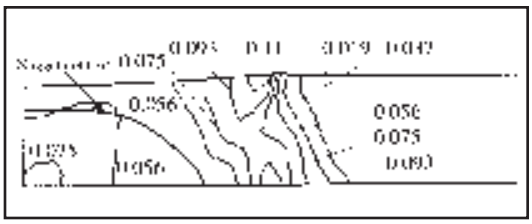

Fig. 8 — Equivalent plastic strain distribution and final weld shape.

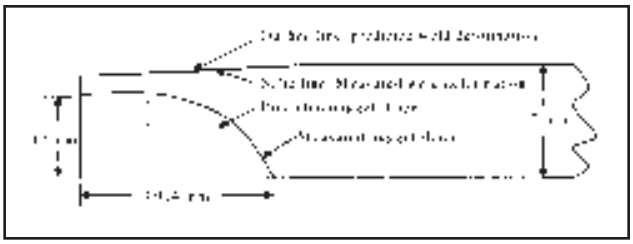

Fig. 9 — Comparison of prediction and measurement.

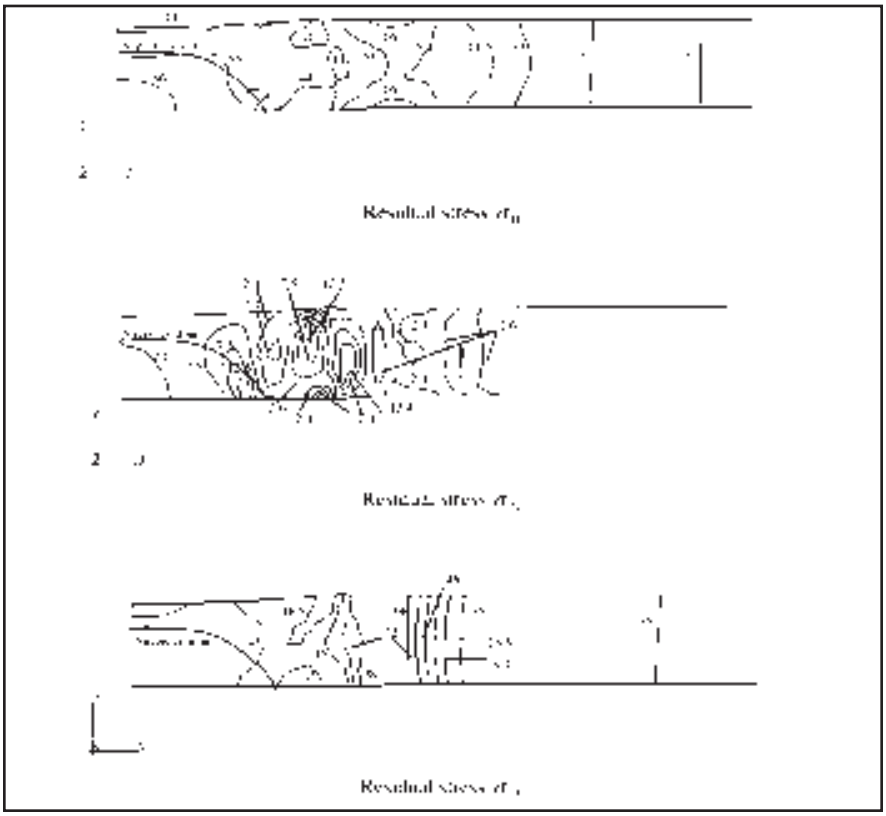

Fig. 10 — Weld residual stress distributions (MPa).

able information on the electrode wear mechanisms and in-process monitoring parameters.

A Case Study

Using the analysis procedures described above, a case study is presented in this section. A typical 2-in.-radius, faced-truncated cone electrode was used to weld 2.0-mm-thick 5xxx series aluminum sheets. The axisymmetric model used in both electro-thermal and thermal-mechanical analyses is shown in Fig. 1. The welding schedule used was listed in Table 1 (Ref. 17).

Four-node axisymmetrical elements were used for mechanical analysis and electrical-thermal analysis. The updating frequency used was half cycle, and the effect of more frequent updating was also examined. Temperature-dependent material properties were used for both the workpieces and the copper electrodes (Refs. 11, 22). Large deformation effect was also considered in the model. The cooling water temperature was set to be 20°C and convection effect was modeled by film coefficient of 2.0×10^{-3} Joule/(s•mm•°C). Notice the present study did not include any material coating effects or the effect of the aluminum-oxide layer.

Nugget Growth

Figure 4 shows the comparison of the predicted nugget size and the nugget size obtained from experimental nugget growth data. The solid symbols represent cross-section measurements of the fusion-zone size from experiments (Ref. 17), while the empty symbols represent the analysis predictions sampled for each half cycle. Given the inherent process variations in aluminum RSW, the overall agreement is considered satisfactory.

A set of parametric studies has also been performed in which the welding current and electrode force are systematically varied. It is found that, as a general trend, a higher current level produces a bigger nugget, as expected. A lower electrode force yields a bigger nugget for the cases analyzed. However, it should be noted sufficient electrode force is needed to generate enough faying interface pressure that can contain the molten metal and prevent expulsion. The underlying principle for RSW is Joule heating, in which the heat is generated in the form of $Q = I^2Rdt$. Therefore, higher current generates more heat and forms a bigger nugget. On the other hand, the decrease of electrode force would reduce the contact area and, in turn, increase the current density. Plus, the contact electrical conductivity of the faying interface will also decrease for a smaller electrode force; these factors will jointly lead to a bigger nugget.

Since this incrementally coupled procedure is mimicking the fully coupled spot welding process, higher updating frequency theoretically should provide more accurate results. In this case study, it was found that updating every quarter cycle only provides higher temperature distribution during the first two cycles and the final nugget size and shape are the same as those of updating every half cycle. It is therefore concluded that updating frequency of a half cycle is sufficient in obtaining the final nugget under this set of welding conditions.

Contact Area Evolution

The contact area change during welding is plotted in Fig. 5. Using this radius-faced electrode, a gradual increase of the contact area between the faying interface and the electrode-sheet interface is obtained as a result of the continued softening of the aluminum sheets as temperature increases. The final contact radii are almost the same for the two interfaces at the value around 4.8 mm. The contact area evolution leads to the changes in current density distributions on the interfaces during welding and would subsequently cause different heating patterns on these interfaces.

Temperature and Pressure Evolution

Because of the changes in contact area, there are also changes in contact pressure distribution. Figure 6 depicts the pressure and temperature evolution history of the electrode-sheet interface. It is shown that the point of highest contact pressure moves from r = 2.8 mm (first cycle) to r = 4.0 mm (ninth cycle) during welding time and there is a temperature drop just outside these peak pressure location for each welding cycle. Inside the peak pressure location, interface temperature is more evenly distributed; this is especially true during the early stage of the welding cycle. These peak pressure points also correspond to the location of maximum plastic strains on the workpiece during welding. The combination of this plastic deformation, higher pressure and temperature concentration facilitates the interdiffusion of copper and aluminum and, therefore, provides a favorable condition for some surface alloys to be formed. This in turn suggests electrode wear is more likely to initiate around this radial location, starting from the middle of the electrode diameter, and subsequently moving out toward the electrode periphery during welding (Ref. 18). The result may be used to explain the electrode surface sticking and pitting phenomenon. It is also worthwhile to mention this analysis is only done for the first weld of the electrode. With subsequent welds, this effect will become more prominent because of the more concentrated heating with the presence of surface alloy and/or pit.

Figure 7A shows the backscatter electron image of a typical weld surface using the welding conditions listed in Table 1. The brighter area represents the location of the copper-rich area on the weld surface. It can be seen that the area of copper concentration corresponds rather well to the prediction of r = 2.8 ~ 4.0 mm. The presence of copper on the aluminum workpiece indicates the electrode is losing material into the weld surface, and the present result can provide explanations for the electrode pitting phenomenon. Figure 7B shows the photograph of a worn electrode face with surface alloying and pitting occurring at the ring location discussed above (Ref. 18). A more detailed study on this subject is currently ongoing and will be reported separately elsewhere.

Deformation and Residual Stresses

Figure 8 shows the equivalent plastic strain distribution after the weld cools to room temperature. Noticeable weld indentation and sheet-to-sheet separation are observed. The final plastic strain on the sheet is concentrated at the periphery of the electrode-to-sheet contact. The predicted sheet indentation at the center of the weld is 6.7% vs. the experimental result of 7.0%. Figure 9 shows the comparison of nugget shape and weld deformation between the prediction and the measurement.

Tensile radial residual stress (σ_{11}) of a magnitude around 70 MPa is predicted for the center of the nugget and the areas outside the electrode periphery on the sheet surface — Fig. 10. This tensile residual stress at the weld center may cause a grain boundary opening that would promote through-thickness nugget cracking (Refs. 14, 18). Through-thickness residual stress (σ_{22}) is found to be of a smaller magnitude, with a peak value around 17 MPa, as expected. The tensile regions are at the nugget periphery on the faying interface and the locations just beneath the electrode periphery on the sheets. This distribution is similar in qualitative manner to the residual stresses obtained by Dong, *et al.* (Ref. 15), for steel, although the residual stress magnitude for aluminum is smaller due to its low yield strength. Circumferential

tensile residual stress (σ_{33}) of a magnitude around 100 MPa is observed at the region just outside the electrode periphery, and its distribution is almost uniform through the sheet thickness. The tensile residual stresses in some of the region form favorable conditions for crack initiation, and further investigations will be conducted to evaluate the implications on weld quality and mechanical performance.

Conclusions

In this paper, an incrementally coupled finite element analysis procedure is presented with a reference specific to the electrical-thermal-mechanical phenomena associated with the aluminum RSW process. Unlike most of the previous efforts in this subject area, which either do not include the coupled effect or only consider the contact area changes, this study takes into account the contact area changes as well as the deformation history effects of the sheet assembly being welded.

To demonstrate the application of the current approach, a detailed case study on welding of the 5xxx series of aluminum alloys is presented. The analysis procedures are validated by experimentally measured nugget growth data. The major findings can be summarized as follows:

- The interfacial contact behavior in the form of contact area change during welding time plays a critical role in the nugget formation process in welding aluminum alloys.
- The predicted pressure and temperature evolution histories on the electrode-sheet interface offer fundamental understanding of electrode pitting and alloy formation mechanisms.
- It is found that, within the range analyzed, lower electrode force or higher welding current generates a bigger nugget.
- Weld residual stresses and final sheet deformation are predicted as measures of weld quality.

Variations of process parameters during welding, such as electrode movements and dynamic resistance, can also be monitored during the welding simulation. These predictions offer a great deal of insight on the mechanisms for nugget formation and electrode wear, and the analysis procedure can be used as a predictive tool to optimize the electrode design and welding parameters to ultimately improve weld quality and reduce electrode wear.

References

1. Greenwood, J. A. 1961. Temperatures in spot welding. *BWRA Report*, pp. 316–322.

2. Han, Z., Orozco, J., Indacochea, J. E., and Chen, C. H. 1989. Resistance spot welding: a heat transfer study. *Welding Journal* 68(9): 363-s to 371-s.

3. Cho, H. S., and Cho, Y. J. 1989. A study of the thermal behavior in resistance spot welds. *Welding Journal* 68(6): 236-s to 244-s.

4. Nied, H. A. 1984. The finite element modeling of the resistance spot welding process. *Welding Journal* 63(4): 123-s to 132-s.

5. Browne, D. J., Chandler, H. W., Evans, J. T., and Wen, J. 1995. Computer simulation of resistance spot welding in aluminum: part I. *Welding Journal* 74(10): 339-s to 344-s.

6. Browne, D. J., Chandler, H. W., Evans, J. T., James, P. S., Wen, J., and Newton, C. J. 1995. Computer simulation of resistance spot welding in aluminum: part II. *Welding Journal* 74(12): 417-s to 422-s.

7. Tsai, C. L., Jammal, O. A., Papritan, C., and Dickinson, D. W. 1992. Modeling of resistance spot weld nugget growth. *Welding Journal* 71(2): 47-s to 54-s.

8. Sheppard, S. D. 1990. Thermal and mechanical simulations of resistance spot welding. *WRC Bulletin 356*, pp. 34–41.

9. Murakawa, H., Kimura, F., and Ueda, Y. 1997. Weldability analysis of spot welding on aluminum using FEM. *Mathematical Modeling of Weld Phenomena*, H. Cerjak, ed., pp. 944–966. The Institute of Materials.

10. Dong, P., Li, M. V., and Kimchi, M. 1997. Analysis of electrode wear mechanisms: Face extrusion and pitting effects. To appear in *Science and Technology of Welding and Joining*.

11. *Metals Handbook*, Vol. 2, 9th ed. 1979. Properties and selections: nonferrous alloys and pure metals.

12. *Welding Handbook*, Vol. 3, 7th Ed. 1980. Resistance and solid-state welding and other joining processes. W. H. Kearn, ed., pp. 2–23.

13. *ABAQUS Theory Manual*, Version 5.5. 1995. Hibbitt, Karlsson & Sorensen, Inc.

14. Watanabe, G., and Tachikawa, H. 1995. Behavior of cracking formed in aluminum alloy sheets on spot welding. *IIW Doc. No. III-1041-95*.

15. Dong, P., Kimchi, M., and Holmes, S. 1995. Thermomechanical analysis of electrode wear mechanisms: A finite element study. *Proc. 11th Annual North American Welding Res. Conf.: Advances in Welding Technology*, pp. 145–162.

16. Li, M. V., Dong, P., and Kimchi, M. 1999. A contact resistance model for coupled finite element simulation of resistance spot welding processes. To appear in *Welding Journal*.

17. Sun, X., Dong, P., and Kimchi, M. 1997. The coupled electrical-thermal-mechanical process associated with aluminum RSW. *Proc. 7th Intl. Conf. Comp. Tech. Welding*, T. Siewert, ed. NIST Special Publication 923, pp. 447–457.

18. Sun, X., Dong, P., and Kimchi, M. 1997. Electrode-sheet interactions during resistance spot welding of aluminum. *Body Assembly and Manufacturing, Proceedings of the International Body Engineering Conference (IBEC)* 30: 42–48.

19. Vogler, M., and Sheppard, S. 1993. Electrical contact resistance under high loads and elevated temperatures. *Welding Journal* 72(6): 231-s to 238-s.

20. Zhang, H., Huang, Y. J., and Hu, S. J. 1996. Nugget growth in resistance spot welding of aluminum alloys. *Proc. 7th Sheet Metal Welding Conf.* Paper B3.

21. Fenech, H., and Rohsenow, W. M. 1963. Prediction of thermal conductance of metallic surfaces in contact. *Journal of Heat Transfer, Trans. ASME* 85(2): 15–24.

22. Rohsenow, W. M., and Hartnett, J. P. 1973. *Handbook of Heat Transfer*. McGraw-Hill Book Company.